

Transcranial Thermoacoustic Tomography: A Comparison of Two Imaging Algorithms

Zijian Liu, Lanbo Liu*, Yuan Xu, and Lihong Victory Wang, *Fellow, IEEE*

Abstract—Thermoacoustic tomography (TAT) is a novel, non-invasive medical imaging technique but has encountered obstacles in imaging through the cranium. In this paper we present two methods for transcranial TAT: Kirchhoff migration (KM) and reverse-time migration (RTM). The two methods' imaging qualities are verified and compared based on both synthetic and experimental data. RTM proves to have better velocity variance and imaging quality, and little noise with spatial aliasing. RTM is a promising approach for achieving transcranial TAT in further studies.

Index Terms—Kirchhoff migration, reverse-time migration, thermoacoustic tomography.

I. INTRODUCTION

THERMOACOUSTIC tomography (TAT) [1]–[3] is a novel, noninvasive medical imaging technique that detects the large differences in microwave absorption between pathological and normal tissue [4], [5]. It applies the principle of the thermoacoustic effect [6], in which an input microwave impulse stimulates thermo-expansion in tissue and consequently generates acoustic waves to be recorded by transducers arranged outside the tissue. When the tissue is relatively uniform, the initial local acoustic amplitude is approximately proportional to the absorption ratio of the microwave [1], [6], [7]. Consequently, the TAT imaging problem is to retrieve the distribution of the initial acoustic amplitude based on recorded acoustic wave energy, and thus it can be characterized as a problem of “source localization.” In recent years, TAT has been widely studied on the imaging of kidney [8], breast [9] and brain [10]–[12]. TAT has been studied for brain imaging for two reasons. First and far more important, TAT takes advantage of deep penetration of the electromagnetic impulse and the high

resolution of the ultrasonic wave for deep imaging. Second, brain tissue is fundamentally uniform and isotropic. For example, the acoustic velocity of human brain is narrowly ranged within 1483–1521 m/s [13]. Acoustic wave propagation inside the brain is very close to one-way line-of-sight transmission without much aberration. The most commonly used imaging algorithm of TAT is to back-project the wave energy recorded by each transducer along the ray paths to all possible locations inside the imaging domain [1], [19]. This method is also known as Kirchhoff migration (KM) [14]–[17] in exploration seismology. Zhu and Lines [18] reported that KM is well performed on its simple scheme with high cost-effectiveness. However, the approximation of one-way sight transmission used in the back-projection algorithm is no longer valid when high velocity contrast exists, for example, when the skull with an acoustic speed of 2500–2900 m/s [19] is included in the imaging domain. For compensating skull-related aberration Jin *et al.* [12] have developed a strategy based on the approximation of ray-tracing; however, it may still suffer from the difficulty of accurately calculating Green's function when the velocity structure becomes more irregular.

In recent years, reverse-time migration (RTM) has emerged as a more precise and powerful imaging tool in the exploration geophysics community [20]–[23]. RTM takes full advantage of the wave equation that includes all the dynamic features of a propagating wave field. Different from KM, RTM is based on the insensitivity of the wave equation's solution to the directionality of time. During RTM, by solving the wave equation with either the finite-differences time domain (FDTD) method [24] or the pseudo-spectral time domain (PSTD) method [25], all transducers act as a virtual source by broadcasting their own records back to the domain in a time-reversed manner. If the velocity model is precise, the reversed-time wave field should converge and be enhanced at the origins of the to-be-imaged structures. Previous studies [18], [26] have compared KM and RTM by using complex velocity structure models, and have confirmed better results by using RTM.

Based on our previous studies [27], [28], in this paper we apply both KM and RTM to a synthetic dataset derived from a 2-D brain model and real datasets acquired from laboratory experiments by Xu and Wang [10] (hereinafter referred as XW06) on rhesus monkey heads. The comparison of imaging results derived by both methods supports the finding of previous studies that RTM is superior to KM in imaging quality and accuracy.

The paper is organized as follows. We demonstrate the application of the two migration methods to synthetic data in Section II and to real laboratory data in Section III. In Section II, we first describe the procedure of building up the 2-D brain

Manuscript received August 24, 2012; accepted October 03, 2012. Date of publication October 12, 2012; date of current version January 30, 2013. This work was supported by the U.S. Department of Defense under Grant W913E5-07-C-008. *Asterisk indicates corresponding author.*

Z. Liu was with the Biomedical Engineering Program, University of Connecticut, Storrs, CT 06269 USA. He is now with Petroleum Geo-Services, Houston, TX 77077 USA (e-mail: zijian.liu@pgs.com).

*L. Liu is with the Department of Civil and Environmental Engineering, University of Connecticut, Storrs, CT 06269 USA (e-mail: lanbo@engr.uconn.edu).

Y. Xu is with the Department of Physics, Ryerson University, Toronto, ON, M5B 2K3 Canada (e-mail: yxu@ryerson.ca).

L. V. Wang is with the Department of Biomedical Engineering, Washington University, St. Louis, MO 63130 USA (e-mail: lhwang@biomed.wustl.edu).

Color versions of one or more of the figures in this paper are available online at <http://ieeexplore.ieee.org>.

Digital Object Identifier 10.1109/TMI.2012.2224667

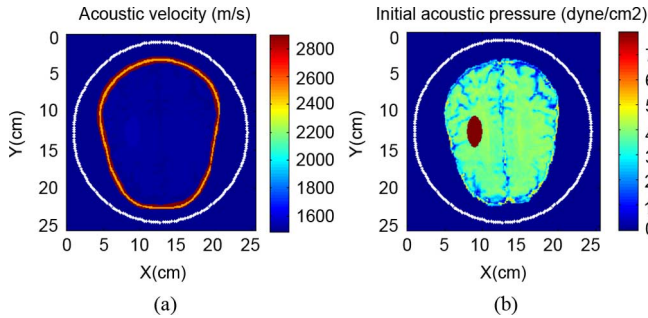


Fig. 1. Layout of the 2-D human brain model with intact skull, where (a) is the distribution of acoustic velocity in the model, in which the skull exhibits relatively higher velocity. The white dots show the locations of the 240 receivers. (b) Amplitude of the initial acoustic pressure stimulated by microwaves during TAT transcranial diagnosis.

models and generating synthetic data by using the FDTD algorithm. Then, applying both KM and RTM to these synthetic data, we present detailed comparison results. In Section III, we first briefly review the acquisition of the laboratory data sets in XW06, then present the imaging results obtained from both methods based on the real data [10] in detail. Section IV is a detailed discussion comparing the results from the two methods in all pertinent aspects. Finally, in Section V we restate the major findings and lay out the direction for future studies.

ALGORITHM VALIDATION VIA SYNTHETIC DATA

To test the effectiveness of KM and RTM, we have built a 2-D synthetic human brain model with an intact skull. In this model, the brain is made of gray matter and white matter [13], and the skull is made of three layers, namely the inner table, diploe, and outer table [19]. To mimic a real laboratory experiment similar to [10], [12], we modeled the space outside the skull as mineral oil, with a uniform acoustic speed. Additionally, to mimic pathological changes and build a benchmark for results analysis, in the synthetic model we replaced a small area of the brain with blood. This area was located at the left cerebral hemisphere and defined as elliptically-shaped. The distribution of acoustic velocity in the synthetic model is shown in Fig. 1(a). From a review of several literatures, mechanical parameters of all related bio-tissues were collected and are listed in Table I, in which the velocities and densities of grey matter and white matter were measured from lamb brain using acoustic frequency of 1 MHz [13]. The skull's velocities, densities and thicknesses of different layers are applied from datasets in research [19], [29] and [30]. The loss factor is defined in [30] to depict the amplitude of the propagating acoustic wave's energy decay. Its values come from [13] for brain and [30] for skull, respectively.

After establishing the mechanical properties, we calculated the initial acoustic amplitudes in the synthetic model. We assumed that the initial acoustic pressure (dyne/cm^2) in mineral oil and the skull was 0, so the acoustic wave field was entirely generated by multiple acoustic sources in the brain at time zero. Their amplitudes were closely linked to the microwave absorption ratio. As expressed in [6], the relationship between the power intensity I (W/cm^2) of absorbed microwaves and the generated peak acoustic pressure P_0 (dyne/cm^2) is shown as

TABLE I
SELECTED MECHANICAL PARAMETERS OF HUMAN BRAIN AND SKULL

Parameter Bio-Material	Density (kg/m^3)	Acoustic speed (m/s)	Loss factor	Thickness (mm)
Grey matter	1039	1483	0.0046	-
White matter	1044	1521	0.0069	-
Outer Table	1870	2900	0.1542	2.0
Diploe	1740	2500	0.1234	2.5
Inner Table	1910	2900	0.1985	1.7
Blood	1057	1500	0	-
Mineral oil	900	1437	0	-

TABLE II
SELECTED ELECTRICAL CONDUCTIVITIES OF HUMAN'S BRAIN

	σ (Sm^{-1}) in 900 MHz	σ (Sm^{-1}) in 1800 MHz
White matter	0.665	1.081
Grey matter	1.009	1.525
Blood	1.868	2.283

(1), where c is the sound velocity, β is the volumetric thermo-expansion coefficient, and C_p is heat capacity. The definition of absorbed power intensity I can be expressed as (2) [7], where E , ρ , and σ are the maximum amplitude of the radiated electromagnetic field, tissue's density, and electrical conductivity, respectively. By combining (1) and (2), (3) is derived as the theoretical relationship between tissue's electrical conductivity and initial acoustic pressure generated based on the thermo-acoustic effect

$$P_0 = \frac{c\beta I}{C_p} \quad (1)$$

$$I = \frac{\sigma}{2\rho} |E|^2 \quad (2)$$

$$P_0 = \frac{\beta c \sigma}{2c_p \rho} |E|^2. \quad (3)$$

The volumetric thermo-expansion coefficient β and heat capacity C_p of the brain are nearly uniform: ($\beta = 12.3 \times 10^{-5}/^\circ\text{C}$ [28] and $C_p = 4160 \text{ KJ/m}^3\text{ }^\circ\text{C}$ [32]). The acoustic velocity and density vary little among gray matter, white matter, and blood (Table I). Nevertheless, the electromagnetic property inside the skull can be estimated as uniform [33]. Consequently the initial acoustic pressure can be well approximated as proportional to the electrical conductivity σ . On the other hand, Table II shows that for input microwaves the electrical conductivities of white matter, gray matter, and blood are significantly different [7]. For blood in particular, σ can be more than 1.5 times higher than for the other two kinds of tissue. Using the value of electrical conductivity for microwave of 900 MHz from [7] and (3), the distribution of initial acoustic pressure is derived, as shown in Fig. 1(b).

Once the synthetic model was established, we applied the FDTD method to forward modeling acoustic wave propagation. Using the initial acoustic pressure shown in Fig. 1(b), a zero-offset Ricker wavelet with a central frequency of 0.15 MHz was applied to each point of the brain as the acoustic source. The model space was meshed as 512×512 grids with a spatial interval of 0.5 mm. The time interval was set up as $0.115 \mu\text{s}$ by

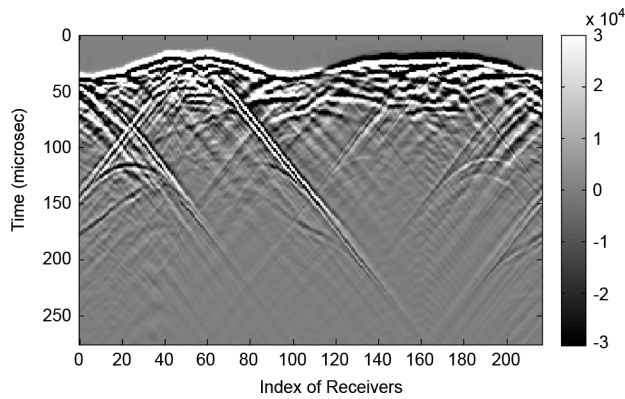


Fig. 2. Acoustic signal recorded during FDTD forward modeling of TAT. This is a cluster with 240 traces, with 1600 samples contained in each trace.

following Courant–Friedrichs–Lewy [34] condition for ensure calculation convergence during FDTD modeling. By referring to Table I, a total of 3000 time steps were estimated to make acoustic waves transmit about 50 cm within the medium of gray matter. This should be long enough to allow the acoustic waves to propagate to each receiver from the most remote grid in our brain model. The outgoing acoustic signal was recorded by 240 receivers located outside the skull (white circle shown in Fig. 1). The synthetic record is shown in Fig. 2, which provides the input dataset for later imaging.

The velocity model used in both migration algorithms is critical to successful imaging. In this study we applied two velocity models: one (abbreviated as V1) assumes the average acoustic velocity is uniformly 1540 m/s in the model space. Essentially it approximates a “bare brain” model with the effect of the skull excluded. The second model (abbreviated as V2) includes the effect of the high acoustic speed of the skull, which is almost double the speed of brain tissues. In our study, velocity models V1 and V2 were applied to both KM and RTM. Due to the velocity variance in V2, we applied V2 to two migration methods by different approaches. In KM, ray-tracing was applied from every transducer to all directions. This procedure was similar to the methods described in [12] but for simplicity we considered only the wave front distortion caused by velocity variance, and ray bending effect around the skull was ignored. Different from KM, as a kind of full-wave migration, RTM uses the same scheme as forward modeling methods such as FDTD. Consequently V2 can be applied to RTM in a straightforward manner. Comparisons of migration imaging results are shown in Figs. 3–5. Need to be noted that the result amplitude derived from KM and RTM appears to be different due to different migration mechanisms, for easier observation all Figs. 3–5 are normalized based on their amplitude on the artificially blooded area.

Fig. 3(a) and Fig. 4(a) are results derived by KM and RTM using the “bare brain” model V1. When compared with the distribution of initial acoustic pressure of the original model [Fig. 3(b) or Fig. 4(b)] we can clearly observe two kinds of imaging artifacts. First, the area with higher initial pressure at the left cerebral hemisphere, which is set up artificially in an elliptical-shape, is seriously enlarged by KM [Fig. 3(a)] and falsely elongated along the major axis of the ellipse by RTM

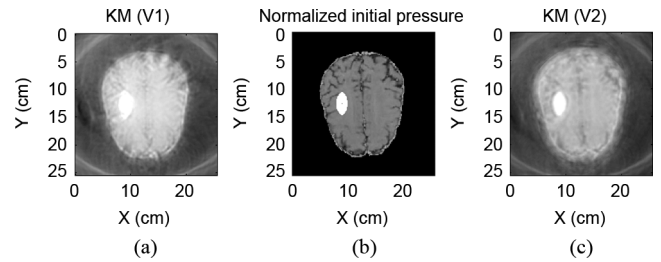


Fig. 3. Comparison among KM results. (a) Results using velocity model V1. (b) Initial acoustic pressure of the original model. (c) KM result using velocity model V2.

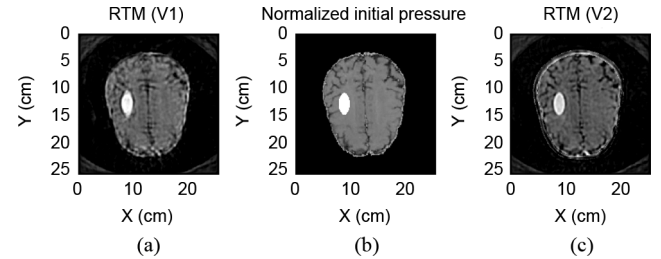


Fig. 4. Comparison among RTM results. (a) Results using velocity model V1. (b) Initial acoustic pressure of the original model. (c) RTM result using velocity model V2.

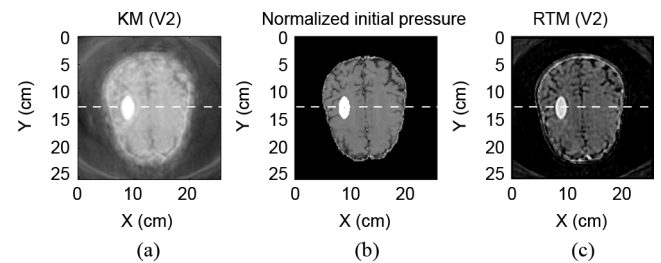


Fig. 5. Comparison among KM results. (a) Results using velocity model V2. (b) Initial acoustic pressure of the original model. (c) RTM result using velocity model V2.

[Fig. 4(a)]. Second, delicate features such as the gyrus, located in the outer part of the brain, and the gap which separates the left and right cerebral hemispheres in our model are totally blurred in both results when using velocity model V1. In contrast, from Fig. 3(c) and Fig. 4(c), which are results based on velocity model V2 with the skull’s velocity included, these two misfits are substantially reduced. From all of these comparisons we can see that exclusion of the skull leads to severe error and distortion in migration imaging for both KM and RTM.

To further examine the differences between KM and RTM, we reorganized the results using KM, RTM, along with the original velocity model V2 as shown in Fig. 5. From it we can see that although both KM and RTM can transform most of the wave field back to its original location correctly, there are obvious differences in imaging quality between the two methods. Compared with the original model shown in Fig. 5(b), the detail features are blurred in KM result [Fig. 5(a)] but appear to be clean and sharp in RTM result [Fig. 5(c)]. These visual differences can be further amplified through 1-D comparison along the x-direction along the horizontal white dashed line shown in Fig. 5 chosen to cross the brain’s left boundary, artificially

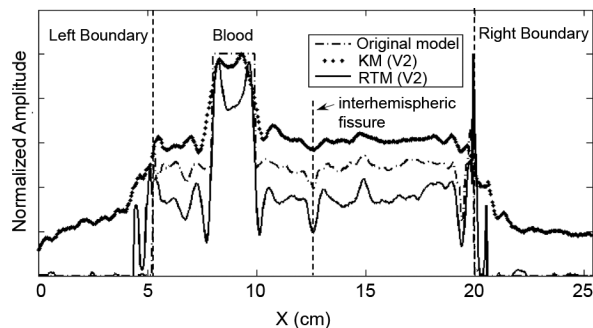


Fig. 6. Cross-sections along the white dashed-line shown in [Fig. 5(a)–(c)], which passes brain's left boundary, artificially blooded area, interhemispheric fissure, and the right boundary. The dotted–broken line, dotted line, and solid line show the original model [Fig. 5(b)], the results by KM [Fig. 5(a)], and RTM [Fig. 5(c)] using the model V2.

blooded area, interhemispheric fissure, and right boundary. The source amplitudes along this profile for KM, RTM, and the original model are shown in Fig. 6. It is obvious that the result of RTM is far more superior than that of KM. Compared with the KM result (the dotted line), result of RTM (the solid line) has larger variance for depicting structures such as interhemispheric fissure around 12.50 cm as well as the boundaries of the artificially blooded area around 7.5 and 10 cm. These differences can also be clearly observed on brain boundaries around 5 and 20 cm, where the amplitude from RTM decays as sharp as the original model, but KM's result is obviously incorrect and decay much slower outside of the brain.

II. APPLICATIONS OF KM AND RTM ALGORITHMS TO LABORATORY DATA

The KM and RTM algorithms were also tested by using the laboratory data acquired by XW06. In their experiment, the monkey's head was decapitated and fixed by a clamp and completely immersed in mineral oil. During TAT detection, a 3-GHz microwave generator transmits $0.5 \mu\text{s}$ microwave pulses at a repetition rate of 20 Hz is applied as a single stimulating source. Microwave energy ($\sim 10 \text{ mJ/pulse}$) is delivered by an antenna with a cross section that gradually changes from $72 \text{ mm} \times 34 \text{ mm}$ to $120 \text{ mm} \times 88 \text{ mm}$. Therefore, the energy flux is on the order of 0.1 mJ/cm^2 at the exit of the antenna. After the specimen was stimulated, the derived acoustic wave field was recorded by a transducer with a 1 MHz central frequency and about 0.8 MHz bandwidth. The transducer was positioned from 6–14 cm to the center of the monkey's head, and the sampling frequency was 20 MHz. During the experiment, the clamp fixing the monkey's head was mounted on a rotary table driven by a stepper motor with a step size of 2.25° . Accordingly in this laboratory application, the outgoing acoustic wave was observed by 160 receivers surrounding the head in a 2-D circle. With data processing performed through the procedure of [35] for high frequency enhancement, only the segment with a spectrum of 0.3–1 MHz of the observed data was picked up and enhanced for imaging by KM and RTM. We applied the estimated average acoustic velocity to both image approaches, since any

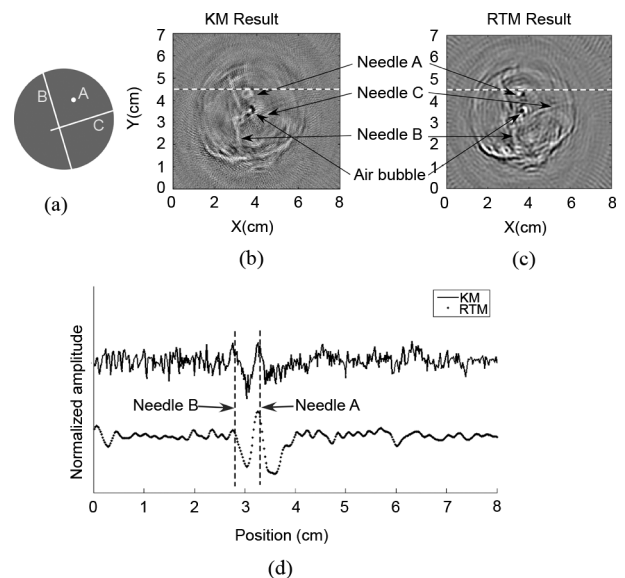


Fig. 7. (a) Diagram showing a monkey head with three inserted needles from XW06. (b) TAT result derived by KM. (c) TAT result derived by RTM. (d) Line plot along the white dashed line at 4.5 cm of (b).

velocity information on velocity distribution of earlier experiment in XW06 was unknown, which may introduce some error and reduce the image quality.

Fig. 7 shows the results based on a dataset collected from a one-month-old monkey head with a skull thickness of less than 1 mm. The region shown is $53 \text{ mm} \times 51 \text{ mm}$ along the coronal cross section. From the experiment of XW06, three steel needles with diameters of 0.9 mm were inserted in the approximate locations as shown in Fig. 7(a) (XW06). The results derived from KM [Fig. 7(b)] and RTM [Fig. 7(c)] are shown side-by-side for comparison. Both imaging algorithms show the three needles, and the black dot located at the center is believed to be an air bubble introduced by inserting the needles (XW06). Compared with the result derived from KM, the result from RTM appears to be less distorted for needle B and with sharper edges on needle A. Meanwhile, KM provides less visibility for needle C than RTM. From the plots along the x cross-section shown in Fig. 7(d), although both needle A and B can be detected by using KM and RTM, the KM image is much noisier. The existence of this noise causes seriously reduction of signal noise ratio and fussy in whole image by KM.

From the experiment using another specimen in XW06, the brain of a seven-month-old monkey was scanned along the coronal cross section through the intact 2-mm-thick skull. The imaging results derived by KM and RTM are shown separately as Fig. 8(a) and (b). In these results several important anatomical features can be identified and used to assess image quality. First, a straight line which starts from the top of brain and goes to right side can be observed from the results of both RTM and KM. This line is suspected to be the superior sagittal sinus. Meanwhile, both results show a horizontal line at the center, which should be the gap between the middle brain and cerebellum. However, due to the thick skull and technical limitations of the coarsely estimated average acoustic velocity for

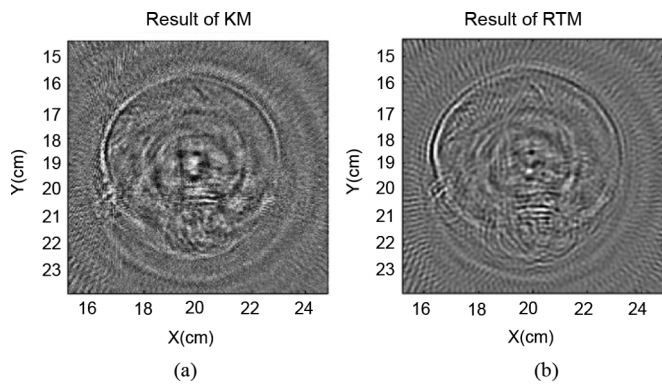


Fig. 8. TAT images derived by different approaches. (a) Result from KM and (b) RTM.

TAT reconstruction, neither of these two methods can provide satisfying image quality.

III. DISCUSSION

It is clear that RTM is superior to KM in terms of imaging quality and higher signal to noise ratio.

Compared with KM, which makes a high-frequency approximation of wave propagation into rays that extract merely the kinematic features of the wave field, RTM bases its entire algorithm on solving a full-wave equation, without substantial approximation, and holds the original dynamic features of the wave field intact. The handle of velocity heterogeneity is fundamentally intrinsic. Usually, adapting ray tracing in KM is time consuming and has a limited improvement on image quality. By applying our ray-tracing method with only wave front distortion correction, as shown in Fig. 3(c), even with the skull's velocity included, most image patterns of the gyrus are not completely transformed back to their correct positions by KM; and the elliptical-shaped blood clot is still falsely enlarged, as shown in the cross-section in the x-direction (Fig. 6), in comparison with the original initial distribution of the acoustic amplitude [Fig. 3(b)]. Possibly this misfit could be reduced by applying more advanced ray tracing techniques [12], [36], which correct both wave front distortion and ray bending, however by solving Eikonal equation along the ray path, the associated high computational intensity might make the usage of KM uneconomical. Unlike KM, the quality of RTM's results is independent of the complexity of the velocity model. This feature makes the wave propagation in the domain highly accurate compared with using ray-tracing. As Fig. 4(c) shows, RTM is able to recover almost all features of the brain to their original position when the skull's velocity is included.

RTM can recover a complex structure's boundary sharply. This has been reported by [18], [26] and is proved by our results in Fig. 4. When both velocity models V1 and V2 are used in RTM, the boundaries of tiny features can be clearly seen. Especially, even though obvious distortions exist in the result using V1 [Fig. 4(a)], with the exclusion of the skull, all features are still relatively un-blurred in comparison with the KM results [Fig. 3(a)]. By comparison, looking at the cross-section in Fig. 6, the sharp edges of brain are well recovered by RTM but

seriously smeared by KM. Further, in Fig. 7 when the skull-excluded model is applied, the contour of Needle C is well recovered by RTM but not by KM.

Nevertheless, it is noteworthy that the image quality of RTM is still limited by the precision of the velocity model. Consequently, in future work the key to capitalizing on the benefit of RTM is to build better velocity models before applying migration. The improvement of the velocity model can be achieved by, for example, direct measurement such as ultrasonic transmission tomography [37], or an iterative migration procedure [22]. Improvements may also result from other leading-edge approaches, such as compressive sensing tomography [38].

IV. CONCLUSION

In this paper, we have compared KM and RTM for transcranial TAT imaging. Compared with KM, RTM offers better performance with regard to velocity variance, imaging quality, and noise suppression caused by spatial aliasing. RTM's imaging quality is restricted by the accuracy of the input velocity model, so that the improvement of velocity model is the key for future work. RTM is a feasible approach for achieving transcranial TAT imaging with high quality and accuracy.

REFERENCES

- [1] M. Xu and L. V. Wang, "Time-domain reconstruction for thermoacoustic tomography in a spherical geometry," *IEEE Trans. Med. Imag.*, vol. 21, no. 7, pp. 814–822, Jul. 2002.
- [2] Y. Xu, D. Feng, and L. V. Wang, "Exact frequency-domain reconstruction for thermoacoustic tomography-I: Planar geometry," *IEEE Trans. Med. Imag.*, vol. 21, no. 7, pp. 823–828, Jul. 2002.
- [3] Y. Xu, D. Feng, and L. V. Wang, "Exact frequency-domain reconstruction for thermoacoustic tomography-II: Cylindrical geometry," *IEEE Trans. Med. Imag.*, vol. 21, no. 7, pp. 829–833, Jul. 2002.
- [4] W. Joines, R. Jirtle, M. Rafal, and D. Schaeffer, "Microwave power absorption differences between normal and malignant tissue," *Radiat. Oncol. Biol. Phys.*, vol. 6, pp. 681–687, 1980.
- [5] M. S. Hawley, A. Broquetas, L. Jofre, J. C. Bolomey, and G. Gaboriaud, "Microwave imaging of tissue blood content changes," *J. Biomed. Eng.*, vol. 13, pp. 37–44, 1991.
- [6] K. R. Foster and E. D. Finch, "Microwave hearing: Evidence for thermoacoustic auditory stimulation by pulsed microwaves," *Science*, vol. 185, pp. 256–258, 1974.
- [7] M. Martinez-Burdalo, A. Martin, M. Anguiado, and R. Villar, "Comparison of FDTD-calculated specific absorption rate in adults and children when using a mobile phone at 900 and 1800 MHz," *Phys. Med. Biol.*, vol. 49, pp. 345–354, 2004.
- [8] C. Cao, L. Nie, C. Lou, and D. Xing, "The feasibility of using microwave-induced thermoacoustic tomography for detection and evaluation of renal calculi," *Phys. Med. Biol.*, vol. 55, no. 17, 2010.
- [9] G. Ku, B. D. Fornage, X. Jin, M. Xu, K. K. Hunt, and L. V. Wang, "Thermoacoustic and photoacoustic tomography of thick biological tissues toward breast imaging," *Technol. Cancer. Res. T.*, vol. 4, pp. 559–566, 2005.
- [10] Y. Xu and L. V. Wang, "Rhesus monkey brain imaging through intact skull with thermoacoustic tomography," *IEEE Trans. Ultrason. Ferroelectr. Freq. Control.*, vol. 53, no. 3, pp. 542–548, Mar. 2006.
- [11] J. Gamelin, A. Aguirre, A. Maurudis, F. Huang, D. Castillo, and Q. Zhu, "Curved array photoacoustic tomography system for small animal imaging," *J. Biomed. Opt.*, vol. 13, no. 2, Mar./Apr. 2008.
- [12] X. Jin, C. Li, and L. V. Wang, "Effects of acoustic heterogeneities on transcranial brain imaging with microwave-induced thermoacoustic tomography," *Med. Phys.*, vol. 35, no. 7, 2008.
- [13] S.-C. Lin, S.-J. Shieh, and M. J. Grimm, "Ultrasonic measurements of brain tissue properties," in *Center Disease Control Conf. Pre-Proc.*, 1997, pp. 27–31.
- [14] W. A. Schneider, "Developments in seismic data processing analysis," *Geophysics*, vol. 36, pp. 1043–1073, 1971.

- [15] W. A. Schneider, "Integral formulation for migration in two and three dimensions," *Geophysics*, vol. 43, pp. 49–76, 1978.
- [16] W. S. French, "Computer migration of oblique seismic reflection profiles," *Geophysics*, vol. 51, pp. 961–980, 1975.
- [17] A. J. Berkout, *Seismic Migration Imaging of Acoustic Energy by Wave Field Extrapolation*. New York: Elsevier, 1982.
- [18] J. Zhu and L. R. Lines, "Comparison of Kirchhoff and reverse time migration methods with applications to prestack depth imaging of complex structures," *Geophysics*, vol. 63, pp. 1166–1176, 1998.
- [19] F. J. Fry and J. E. Barger, "Acoustic properties of human skull," *J. Acoust. Soc. Am.*, vol. 63, pp. 1576–1590, 1978.
- [20] C. Hemon, "Equations d'onde et modeles," *Geophys. Prosp.*, vol. 26, pp. 790–821, 1978.
- [21] G. A. McMechan, "Migration by extrapolation of time-dependent boundary values," *Geophys. Prosp.*, vol. 31, pp. 412–420, 1983.
- [22] N. D. Whitmore, "Iterative depth migration by backward time propagation," *Proc. 53rd Ann. Int. Mtg. Soc. Expl. Geophys.*, pp. 827–830, 1983.
- [23] E. Baysal, D. D. Kosloff, and J. W. C. Sherwood, "Reverse-time migration," *Geophysics*, vol. 48, pp. 1514–1524, 1983.
- [24] K. Yee, "Numerical solution of initial boundary value problems involving maxwell's equations in isotropic media," *IEEE Trans. Antennas Propag.*, vol. 14, no. 3, pp. 302–307, May 1966.
- [25] Q. H. Liu, "The PSTD algorithm: A time-domain method requiring only two cells per wavelength," *Microw. Opt. Technol. Lett.*, vol. 15, no. 3, pp. 158–165, Jun. 1997.
- [26] P. Farmer, Z. Zheng, and D. Jones, "The role of reverse time migration in imaging and model estimation," *Geophysics*, vol. 28, pp. 436–441, 2009.
- [27] Z. Liu and L. Liu, "A novel approach for thermoacoustic tomography by Kirchhoff migration," presented at the 9th Int. Conf. Theoretical Computational Acoust., Dresden, Germany, 2010.
- [28] L. Liu, K. He, and L. V. Wang, "Transcranial ultrasonic wave propagation simulation: Skull insertion loss and recovery," presented at the SPIE Conf., San Francisco, CA, 2007.
- [29] N. Lynnerup, J. G. Astrup, and B. Astrup, "Thickness of the human cranial diploe in relation to age, sex and general body build," *Head Face Med.*, pp. 1–13, 2005.
- [30] M. Hayner and K. Hynynen, "Numerical analysis of ultrasonic transmission and absorption of oblique plane waves through a human skull," *J. Acoust. Soc. Am.*, vol. 110, pp. 3319–3330, Dec. 2001.
- [31] J. C. Lin, "Microwave-induced hearing: Some preliminary theoretical observations," *J. Micro. Power*, vol. 11, no. 3, 1976.
- [32] X. Xu, P. Tikuisis, and G. Giesbrecht, "A mathematical model for human brain cooling during cold-water near-drowning," *J. Appl. Physiol.*, vol. 86, pp. 265–272, 1999.
- [33] R. Huber, J. Schuderer, T. Graf, K. Jutz, A. A. Borbely, N. Kuster, and P. Achermann, "Radio frequency electromagnetic field exposure in humans: Estimation of SAR distribution in the brain, effects on sleep and heart rate," *Bioelectromagnetics*, vol. 24, pp. 262–276, 2003.
- [34] R. Courant, K. Friedrichs, and H. H. Lewy, "On the partial difference equations of mathematical physics," *IBM J.*, vol. 11, pp. 215–234, 1967.
- [35] Y. Xu and L. V. Wang, "Signal processing in scanning thermoacoustic tomography in biological tissues," *Med. Phys.*, vol. 28, pp. 1519–1524, Jul. 2001.
- [36] S. Schmidt, O. Roy, C. Li, N. Duric, and Z. Huang, "Modification of Kirchhoff migration with variable sound speed and attenuation for tomography imaging of the breast," *Proc. SPIE*, vol. 7968, 2004.
- [37] X. Jin and L. V. Wang, "Thermoacoustic tomography with correction for acoustic speed variations," *Phys. Med. Biol.*, vol. 51, pp. 6437–6448, 2006.
- [38] Z. Guo, C. Li, L. Song, and L. V. Wang, "Compressed sensing in photoacoustic tomography in vivo," *J. Biomed. Opt.*, vol. 15, no. 2, 2010.